

RSC Advances



This is an *Accepted Manuscript*, which has been through the Royal Society of Chemistry peer review process and has been accepted for publication.

Accepted Manuscripts are published online shortly after acceptance, before technical editing, formatting and proof reading. Using this free service, authors can make their results available to the community, in citable form, before we publish the edited article. This *Accepted Manuscript* will be replaced by the edited, formatted and paginated article as soon as this is available.

You can find more information about *Accepted Manuscripts* in the [Information for Authors](#).

Please note that technical editing may introduce minor changes to the text and/or graphics, which may alter content. The journal's standard [Terms & Conditions](#) and the [Ethical guidelines](#) still apply. In no event shall the Royal Society of Chemistry be held responsible for any errors or omissions in this *Accepted Manuscript* or any consequences arising from the use of any information it contains.

1 Synergistic Strategies for the Preparation of Highly
2 Efficient Dye-Sensitized Solar Cells on Plastic
3 substrates: Combination of Chemical and Physical
4 Sintering

5 *Yuelong Li^{a,b,†}, Kicheon Yoo^{a,c,†}, Doh-Kwon Lee^{a,d}, Jin Young Kim^a, Hae Jung Son^a, Jong Hak*
6 *Kim^c, Chul-Ho Lee^e, Hernán Míguez^{b,*}, Min Jae Ko^{a,d,e,*}*

7 ^aPhoto-Electronic Hybrids Research Center, Korea Institute of Science and Technology, Seoul
8 02792, Republic of Korea

9 ^bInstituto de Ciencia de Materiales de Sevilla, Consejo Superior de Investigaciones Científicas,
10 Avda. Américo Vespucio 49, 41092 Sevilla, Spain.

11 ^cDepartment of Chemical and Biomolecular Engineering, Yonsei University, 120-746, Korea

12 ^dGreen School, Korea University, 145, Anam-ro, Seongbuk-gu, Seoul 02841, Korea

13 ^eKU-KIST Graduate School of Converging Science and Technology, Korea University, Seoul
14 02841, Republic of Korea

15

1 **ABSTRACT:** Preparation of well-interconnected TiO₂ electrodes at low temperature is critical
2 for the fabrication of highly efficient dye-sensitized solar cells (DSCs) on plastic substrates.
3 Herein we explore a synergistic approach using a combination of chemical and physical
4 sintering. We formulate a binder-free TiO₂ paste based on “nanoglue” as the chemical sintering
5 agent, and use it to construct a photoelectrode on plastic by low-temperature physical
6 compression to further improve the connectivity of TiO₂ films. We systematically investigated
7 the factors affecting the photovoltaic performance and found the conditions to achieve electron
8 diffusion lengths as long as 25 μm and charge collection efficiencies as high as 95%, as
9 electrochemical impedance spectroscopy measurements indicate. We apply this approach to
10 obtain a DSC deposited on plastic displaying 6.4% power conversion efficiency based on
11 commercial P25 titania particles.

12
13 **KEYWORDS:** dye-sensitized solar cells; nanoglue; low-temperature sintering; chemical
14 sintering; physical sintering; interconnection of particles; hot compression method;
15 electrochemical impedance spectroscopy.

16
17
18
19
20
21
22

1 INTRODUCTION

2 Flexible dye-sensitized solar cells (DSCs) have attracted great interest from scientific
3 researchers¹⁻¹⁵ around the world, as flexible DSCs could be used as portable and mobile
4 ubiquitous power suppliers and satisfy the requirements for continuous roll-to-roll, high volume
5 manufacturing processes needed for future commercialization. For the fabrication of the high
6 performance flexible DSCs on a plastic substrate, considerable efforts have been made to
7 enhance the tight interconnection of TiO₂ nanoparticles at low temperature ($\cong 150^{\circ}\text{C}$) because
8 the plastic substrates cannot withstand the conventional sintering temperature of approximately
9 500°C. Up to now, many low temperature fabrication processes have been reported, and most of
10 them can be categorized into chemical and physical sintering methods. As for the latter, the
11 compression¹⁶ method has been considered as a quick and simple technique to fabricate well
12 interconnected TiO₂ film for highly efficient DSCs on plastic substrates.¹⁷ Recently, we
13 developed novel chemical sintering method using the concept of an inorganic interparticle
14 agent,^{5, 6} coined “nanoglue”, for inducing the chemical bonding of neighboring TiO₂
15 nanoparticles during thermal treatment; this allowed to build cells that reached 5.4% efficiency at
16 the low temperature of 130 °C so to preserve the thermal stability of the plastics involved.
17 Although there have been several studies on the individual effects of chemical and physical
18 sintering effect on the performance of plastic DSCs, there is few report on the plastic DSCs
19 prepared from both physical and chemical sintering methods. It would be of great interest to
20 combine the compression, or physical sintering with the nanoglue based chemical sintering, for
21 the preparation of highly efficient DSCs on plastic substrates.

22

1 In this manuscript, we analyze the effect of combining chemical sintering with physical
2 sintering and demonstrate plastic supported solar cells that reach a power conversion efficiency
3 of 6.4% based on commercial available P25 titania particles, which is quite state-of-the-art value
4 compared with that of previously published based on the home-made titania particles. This
5 synergic strategy relies on the use of a binder-free paste containing *nanoglue* and then
6 compression simultaneously with being sintered at 130 °C. Systematic investigation of the
7 factors affecting the performance of DSCs prepared by this combined method was carried out;
8 the optimum pressure applied on the glued nanocrystalline pastes to maximize electron diffusion
9 length and collection was found.

10 **EXPERIMENTAL**

11 20 wt% TiO₂ particles (P25, 21 nm, Degussa) in ethanol solution were dispersed by Ultra
12 Apex Mill (Model UAM-015, Kotobuki). An interparticle binding agent, or nanoglue, was
13 synthesized by a sol-gel process following a published procedure.⁵ Anatase TiO₂ particles of 5
14 nm size were added to the nanoglue to induce good interparticle connection at low temperature.
15 Large TiO₂ particles (T030, 320 nm, K. K. Titan, Japan) were used to cause multiple scattering
16 within the electrode and hence enhance light harvesting.

17 The viscous binder-free paste was prepared according to the following procedure: dispersed
18 P25 particles, small particles from nanoglue gel and large T030 particles were mixed and
19 dispersed by tip sonication (Q500 Sonicator, Qsonica) followed by vigorous shaking with a
20 vortex mixer for at least 10 min each. The weight ratio of particles of P25: T030: nanoglue is
21 optimized to 55:30:15. The solid content of the particle mixture in the final pastes was fixed at
22 15 wt%.

1 The TiO₂ films were spread using a doctor blade onto a transparent conducting plastic
2 substrate (ITO/PEN, 200- μ m-thick, 15 Ω /sq, transmittance of 80% at 550 nm, Peccell Tech. Inc.);
3 3M tape is used as a spacer. After drying at ambient temperature, TiO₂ films were compressed at
4 with temperature of 130 °C for 5 min with a lamination apparatus (Creative & Innovation
5 System, Korea). A thin Teflon film was inserted between the TiO₂ film and the piston to avoid
6 contamination and film removal during compression. Compressed films were immersed into 0.5
7 mM N719 (*cis*-bis(isothiocyanato)-bis(2,2'-bipyridyl-4,4'-dicarboxylato)-ruthenium(II) bis-
8 tetrabutylammonium, anhydrous ethanol solution for dye loading at 40 °C for 3 h with
9 continuous shaking. Pt counter electrode was prepared by spreading a drop of 7 mM of
10 H₂PtCl₆•6H₂O in 2-propanol on a glass substrate (FTO/glass, 8 Ω /sq, 2.3-mm-thick, Pilkington
11 TEC8), drying at ambient temperature and annealing at 400 °C for 20 min. The two electrodes
12 were assembled using 60- μ m-thick hot melt Surlyn (Dupont 1702). The standard electrolyte
13 solution was composed of 0.7 M 1-propyl-3-methylimidazolium iodide (PMII), 0.03 M iodine
14 (I₂), 0.05 M guanidinium thiocyanate (GuSCN) and 0.5 M 4-tert-butylpyridine (tBP) in a mixture
15 of acetonitrile and valeronitrile (v/v = 85:15); it was introduced through the drilled holes on the
16 counter electrode. The active area of the dye-adsorbed TiO₂ films was about 0.45 cm² as
17 measured by an image analysis program equipped with a digital microscope camera (Moticam
18 1000). The thickness of the TiO₂ films was measured by an Alpha-step IQ surface profiler (KLA
19 Tencor).

20 The amounts of dye adsorbed on the TiO₂ films were quantitatively estimated by desorbing the
21 dye in basic solution, as follows: the sensitized films with known areas and thicknesses were
22 rinsed by anhydrous ethanol and then dried in a dry nitrogen flow. The films were immersed in a
23 measured volume of 0.1 M NaOH solution in water/ethanol (50:50 v/v) for 24 h to remove the

1 dye molecules from the TiO₂ films. The UV-Vis absorption spectrum of the resultant solution
2 was recorded using a Perkin-Elmer Lambda 35 UV-Vis spectrometer, as shown in Fig. S1 in the
3 Supporting Information.

4 High-resolution transmission electron images (HR-TEM) were obtained using a Field-
5 Emission-Gun-equipped TEM instrument (FEI Tecnai F20, Philips Electron Optics, Holland).
6 Photocurrent-voltage measurements were performed using a Keithley 2400 source measure unit.
7 A solar simulator (Yamashida Denso) equipped with a 1000-W Xe lamp was used as a light
8 source. Light intensity was adjusted employing an NREL-calibrated Si solar cell. A black mask
9 was placed on top of the cells to prevent diffusion of light during measurement. The incident
10 photon-to-current conversion efficiency (IPCE) was measured using a system specifically
11 designed for DSCs (PV measurements, Inc.). The electrochemical impedance spectra (EIS) were
12 attained in the frequency range of 10⁻¹–10⁶ Hz using a potentiostat (Solartron 1287) equipped
13 with a frequency response analyzer (Solartron 1260); the magnitude of the alternate signal was
14 10 mV. Impedance parameters were determined by fitting the impedance spectrum using Z-view
15 software. The impedance measurements were carried out in the dark by sweeping the applied
16 potential.

17 **RESULTS AND DISCUSSION**

18 The structural and morphological properties of films composed of ternary particles were
19 examined by transmission electron microscopy (TEM). The films were scratched off the
20 substrates and deposited on a microscope grid. In Fig. 1(a), it can be seen that smaller particles,
21 composing the actual nanoglue, fill the voids between the larger P25 and T030 scattering
22 particles, and continuously connect larger particles together to yield a more compact structure
23 which potentially reduce pore size and porosity of resulted films. From the enlarged image in

1 Fig. 1(b), the crystallinity and size of small nanoglue particles can be clearly seen, which is pure
2 anatase phase for crystallinity and about 5 nm for the size. After compression, the morphology
3 and structure of both the surface (left column, Fig. 2) and the cross section (right column, Fig. 2)
4 of the films were characterized by scanning electron microscopy (SEM). It was observed that the
5 ternary particle composition films compressed at 0 MPa, corresponding to film without
6 compression, display a smooth surface without any cracks (Fig. 2(a)), which is a basic
7 requirement to achieve a reasonable cell performance; cracks within a film have a dramatic effect
8 on the electron transport between neighboring particles and hence deteriorate the photovoltaic
9 performance.^{10, 18} Additionally, a mesoporous structure was observed from the cross-view of
10 SEM in Fig. 2(b). More SEM images were obtained of the films pressed at 40 MPa, 100 MPa
11 and 160 MPa in order to examine the effect of applying different and increasing pressures on
12 film morphology. Fig. 2(c) exhibit a film pressed at 40 MPa, it shows that the surface becomes
13 more flat with compression; the effect is more significant for films compressed at 100 MPa and
14 160 MPa, as shown in Fig. 2(e) and (g). The surface roughness of the films was evaluated from
15 the three-dimensional images of atomic force microscopy (AFM). (Fig. S2) The root mean
16 square roughness (R_q) significantly decreases from 47.66 nm for uncompressed film to 15.95 nm
17 for compressed films at 40 MPa, and continues gradually decreasing to 11.71 nm and 5.27 nm
18 for compressed films at 100 MPa and 160 MPa, respectively. The reduced R_q indicates flattened
19 surface by compression. We quantitatively investigated the structural properties related to pore in
20 the film using Barrett-Joyner-Halenda (BJH) pore size and volume analysis. As summarized in
21 Table S1, compressed films hold both smaller pores and less porosity with increasing applied
22 pressure. The reduction of porosity with increasing pressure may be due to the reduction of the
23 interparticle space with the closer packing of the nanoparticles; the packing could partially shift

1 from a relatively loose cubic pileup to the denser tetrahedral pileup as schematized in Fig. S3.
2 According to BJH analysis, the porosity (P) of compressed films are 41.8%, 34.0%, 25.6%, and
3 22.8% for applied pressures of 0 MPa, 40 MPa, 100 MPa, and 160 MPa, respectively, which
4 presents similar tendency with a previous report,⁸ The average nanoparticle coordination number
5 (N) for ternary composition films subjected to different pressures was estimated according to the
6 approximate expression:¹⁹⁻²¹

$$N = (3.08/P) - 1.13 \quad (1)$$

7
8 Values of $N=6.2$, $N=7.9$, $N=10.9$ and $N=12.4$ are obtained for the films compressed at 0
9 MPa, 40 MPa, 100 MPa, and 160 MPa, respectively. For a particle network to be mechanically
10 stable, the average N has to be at least 3.²⁰ Hence, our results are in good agreement with the
11 observation of crack-free films in all cases by SEM.^{20, 21} Furthermore, better electron transport
12 between nanoparticles is expected for structures with higher values of N .

13 The average photovoltaic properties of cells based on compressed films with thickness of
14 about 6.5 μm were summarized in Table 1; graphical representation together with photocurrent-
15 voltage, IPCE curves of these data can also be found in Fig. S4. As clearly seen in Table 1, the
16 cell which was just dried at room temperature in air without compression has the lowest
17 efficiency; we use the photovoltaic parameters values of this cell as our reference. After
18 compression at 40 MPa, the short-circuit current (J_{SC}) of the cells is remarkably enhanced from
19 5.42 mA/cm^2 to 8.46 mA/cm^2 . The J_{SC} continuously increases with increasing compression and
20 reaches a maximum of 9.64 mA/cm^2 at a pressure of 100 MPa; a 78% improvement with respect
21 to the reference is observed. Such significant enhancement in J_{SC} can be attributed to the
22 enhanced interparticle connectivity caused by compression. Interestingly, J_{SC} began to decrease
23 with further increase of compression pressure, as will be discussed later. On the other hand, the

1 open circuit voltage (V_{OC}) increases from 778 mV in the reference cell to approximately 795 mV
2 in the cell in which the electrode is compressed at 40 MPa; no significant variations are observed
3 after further compression. The fill factor (FF) shows similar tendencies to the V_{OC} . The power
4 conversion efficiency (η) follows the same trend as the J_{SC} and a significantly increase from
5 2.86% to 5.31% is observed after compression at 100 MPa. Unlike the significant increase of cell
6 performance from 2.86% for uncompressed cell to 4.66% for compressed cell at 40 MPa, the
7 increment of performance was not so noticeable when higher compression force were applied.
8 This is probably due to the trade-off relationship between interconnectivity of nanoparticles and
9 mass transport (ionic diffusion) of electrolyte in the pores. Higher compression could induce
10 tighter interparticle connection, which is favorable for the electron transport, but at the same time,
11 it could reduce the porosity of films and pores size, which would retard the electrolyte diffusion
12 in the pores. Consequently, the degree of compression affects the cell performance. Under our
13 experimental conditions, compressed cells with 100 MPa always presented the best cell
14 performance and highest average performance, which is in good agreement with previous
15 observations for compressed cells.^{2,10}

16 It is also worth mentioning that the most efficient reference cell reached an efficiency of
17 3.02%, which is comparable or even higher than many published results for films produced with
18 physical compression or sintering treatment;^{22,23} this demonstrates the beneficial effect of using
19 nanoglue in the binder-free paste. The synergic effect of physical compression and chemical
20 sintering was confirmed by evaluating the effect of heating a ternary particle based electrode to
21 130 °C without applying any pressure; a cell displaying a 4.50% power conversion efficiency
22 was obtained. η is well below 5.38% which was attained for a cell with electrodes that had been

1 simultaneously compressed and chemically sintered at 130 °C; comparative data is provided in
2 Table S2.

3 A series of studies were conducted to determine the origin of the enhancement of the
4 photovoltaic properties by simultaneous chemical sintering and compression. Due to its
5 dominant role in determining cell efficiency, parameters affecting the J_{SC} were first considered.
6 J_{SC} is the product of light harvesting by the dye, electron injection (from the excited state of the
7 dye to the conduction band of TiO₂), and charge collection efficiencies.²⁴ The dye load of each
8 compressed electrode was examined according to the procedures described in the experimental
9 section. Fig. 3 is a plot of the dye load and J_{SC} as a function of the compression pressure; it can
10 be seen that even when the dye load was slightly reduced, the J_{SC} gradually increased with
11 compression pressure as the structure densified. As long as the amount of absorber is basically
12 preserved, the observed increase in J_{SC} should be attributed to either improved charge injection
13 or electron diffusion; improved charge injection is not expected to be affected by compression,
14 while electron diffusion depends on the phenomena of electron transport and recombination. The
15 reason for the increase in J_{SC} was investigated using electrochemical impedance spectroscopy
16 (EIS) under one-sun illumination with open circuit and in the dark with applied forward
17 potential. The frequency resolved information at the individual interfaces can be quantitatively
18 investigated by fitting Nyquist plots to proper equivalent models.²⁵⁻²⁷ It is generally known that
19 the semicircles occurring in the range of 10¹–10² Hz and 10²–10³ Hz are related to the charge
20 transfer process at the TiO₂/electrolyte interface and the injection of electrons into the TiO₂
21 films, respectively. The higher frequency semicircles (in the kHz range) are associated with
22 charge transfer at the Pt counter electrode and/or electrical contact between the ITO/TiO₂ films.
23 Semicircles at lower frequencies (less than 10 Hz) represent redox ionic diffusion within the

1 electrolyte²⁸. The impedance spectra were first recorded at one sun illumination with open circuit
2 condition and typical Nyquist plots were obtained (Fig. 4). As seen in Fig. 4 (a), the impedance
3 arc of films produced without compression was a little distorted in the range used for the
4 estimation of electron transport resistance in TiO₂ films.²⁹ The distortion is usually originates
5 from poor connection between TiO₂ nanoparticles and indicates that the electron transport
6 resistance is much greater than charge transfer resistance at the TiO₂/electrolyte interface.¹²
7 Contrarily, all compressed films display the typical three-semicircles, which can be clearly
8 decoupled, implying enhanced interconnection within the TiO₂ photoelectrodes after
9 compression. Spectra were fitted using the equivalent circuit model and the results are
10 summarized in Table S3. The resistance (R_1), estimated from the semicircle at high frequency,
11 generally includes information on the charge transfer at the counter electrode and the electrical
12 contact between TiO₂ and ITO substrates. As the same platinized counter electrodes are used for
13 all cells, differences in R_1 may be mainly ascribed to variations of the electrical contact
14 resistance between the TiO₂ films and ITO substrates. R_1 was significantly reduced from 5.82 to
15 1.89 Ω after simultaneous chemical sintering and compression, highlighting the good adhesion
16 between the TiO₂ films and ITO substrates in the compressed films. The resistance R_2 , extracted
17 from the analysis of the second semicircle, carries information on the charge transfer process at
18 the interface between the TiO₂ and the electrolyte. The relatively higher values of R_2 attained
19 from cells based on compressed films indicate less recombination in the cells with compressed
20 films, which led to a relatively higher observed V_{OC} for cells containing compressed films.
21 Finally, the effect of compression on the diffusion of electrolyte within the TiO₂ films was
22 determined by evaluating the Warburg impedance (W_1). Larger W_1 was found from the films
23 under analysis; this indicates that the reduced porosity resulting from compression hinders ionic

1 diffusion of redox ionic species. The diffusion coefficients (D_R) were also calculated based on
2 the fitted data of low frequency semicircles as follows:²⁸

$$3 \quad D_R = (1/2.5)\delta^2\omega_{max} \quad (2)$$

4 where δ is the cell gap between two electrodes and ω_{max} is the peak frequency of the low
5 frequency arc; a δ of 16 μm is used in this study. According to the calculated results (Table S3),
6 we find that the maximum value of D_R is obtained from films produced without compression.
7 The poorer electrolyte diffusion in compressed films seems to gradually affect the dye
8 regeneration and hence the J_{SC} , especially with compression pressures greater than 100 MPa;
9 poor electrolyte diffusion in the cells with compressed films could also result in a decline of the
10 electron transport behavior in TiO_2 film.

11 Cells were also evaluated by EIS in the dark with a variation of bias voltage using the
12 transmission line model. By interpreting these measurements, in contrast to those realized under
13 illumination with open circuit voltage, electron transport within the TiO_2 network and charge
14 transfer at the interface of TiO_2 /electrolyte could be more clearly evaluated. While decreasing the
15 forward bias potential from 0.75 to 0.55 V, electron transport in the mesoscopic TiO_2 film is
16 characterized by a Warburg-like diffusion behavior in the high-frequency region (a straight line)
17 and mid-frequency region (a large semicircle) corresponding to an interfacial charge
18 recombination processes.^{26, 28, 30} The reaction of photogenerated electrons with the I_3^- ions at the
19 TiO_2 /electrolyte interface typically depends on the transport of both the electrons within the
20 interconnected TiO_2 nanoparticles chains and the redox species throughout the pore network of
21 the mesostructure. If L is the thickness of the TiO_2 film, then the electron transport resistance in
22 the TiO_2 film is $R_t=r_tL$, where r_t is the inter-particle resistance. The overall recombination
23 resistance is $R_{ct}=r_{ct}/L$ where r_{ct} is the charge-transfer resistance opposing the recombination

1 process between electrons in the mesoscopic TiO₂ film and I₃⁻ in the electrolyte. The chemical
 2 capacitance is $C_{\mu}=c_{\mu}L$ where c_{μ} is the inter-particle chemical capacitance. Therefore, the electron
 3 transport and recombination behavior may be quantitatively examined by fitting the Nyquist plot
 4 with ideal characteristics of the diffusion-recombination model with $R_{ct} \gg R_t$ and calculated
 5 according to the equation.^{26, 28}

6 From the fitted data, we could calculate the evolution of parameters such as electron diffusion
 7 coefficient (D_n), electron diffusion length (L_n) and charge collection efficiency (η_{cc}) according to
 8 the following equations.^{30, 31}

$$9 \quad D_n = L^2 / (R_t C_{\mu}) \quad (3)$$

$$10 \quad L_n = L \sqrt{R_{ct} / R_t} \quad (4)$$

$$11 \quad \eta_{cc} = 1 - R_t / (R_t + R_{ct}) \quad (5)$$

12 For an efficient cell, it is essential to have the longer L_n , higher η_{cc} and D_n at any bias voltage
 13 between short circuit and open circuit. A simple illustrative electron transport and recombination
 14 scheme is shown in Fig. 5 (a) based on the fitted R_t and R_{ct} with the calculated D_n , L_n , and η_{cc} . As
 15 forward bias increases, more electrons are injected from the ITO substrate into the TiO₂
 16 conduction bands and the film is further charged by the accumulated electrons through the
 17 mesoscopic TiO₂ nanoparticle networks. The degree of electron accumulation can be reflected by
 18 an upshift of quasi-Fermi level (E_{Fn}) of the TiO₂ films. Therefore, the connectivity of TiO₂
 19 nanoparticles would also affect the shift of E_{Fn} . According to trap-detrap model accounting for
 20 electron transport mechanism in DSCs, the potential difference between E_{Fn} and the conduction
 21 band influences electron transport.³² Hence, if the connectivity of TiO₂ network is good enough,
 22 a relatively smaller forward bias is required to achieve similar R_t as well as E_{Fn} . As shown in Fig.
 23 5(b), less forward bias is required for DSCs prepared with compression until 100 MPa, which

1 constitutes additional evidence of the improved connectivity of TiO₂ nanoparticles. However, it
2 is also observed that higher forward bias is required for cells with electrodes prepared using
3 compression of 160 MPa than those prepared with 40 MPa compression which indicates an
4 increased electron transport resistance under excessive compression. The main reason for
5 slowing electron transport behavior with compression of 160 MPa is probably due to the reduced
6 porosity (22.3%) and pore size (2.36 nm), which retards diffusion of the electrolyte cation
7 through the mesoscopic structure of TiO₂ to neutralize the charged sites on the surface of TiO₂
8 nanoparticles (Table S3); this which gives rise to higher R_t .³³ On the other hand, no significant
9 difference of R_{ct} is observed between the DSCs with compressed films, implying that almost
10 similar recombination events occur for those cells, as shown in Fig. 5(c). Nevertheless, the
11 smallest R_{ct} was obtained from cells made of uncompressed electrodes, which is in good
12 agreement with the V_{OC} trends reported in Table 1. The competition between charge collection
13 and charge recombination in the DSCs can be expressed in terms of D_n , L_n and η_{cc} as displayed in
14 Fig. 5(d), (e) and (f). It can be concluded that cells made of compressed films present better
15 diffusion and cells prepared with an electrode pressed at 100 MPa exhibit the best performance.
16 Additionally, a longer L_n was achieved from the compressed films than has been previously
17 published for electrodes sintered at low temperature.^{6, 34-36}; an L_n of approximately 25 μm was
18 achieved for the best performing cells of compressed films. This result confirms the benefit of
19 the combined effect of chemical and physical sintering. The η_{cc} is evaluated by equation 5;
20 generally, higher η_{cc} is desirable for an efficient solar cell.³¹ As shown in Fig. 5(f), a great
21 improvement of η_{cc} was demonstrated from compressed cells; η_{cc} of 95% was obtained for the
22 cells compressed at 100 MPa. It is concluded that the synergetic approach combining physical
23 sintering and chemical sintering effectively reinforced the connectivity of nanoparticles,

1 resulting in an efficient electron transport through the TiO₂ network. In order to further enhance
2 the efficiency, the thickness of TiO₂ film was tailored from 6.5 μm up to 8.7 μm. By doing so,
3 the J_{SC} increased from 9.67 mA/cm² to 11.02 mA/cm² and led to a 6.38% power conversion
4 efficiency (Fig. 6 (a-b)). The schematic of typical anode made of binder-free titania film is
5 depicted in the Fig. 6(a) together with photovoltaic properties summarized in the inserted table. It
6 is reasonable to expect further improvement of cell performance by replacing commercial P25
7 nanoparticles with better home-synthesized TiO₂ nanoparticles.

8 CONCLUSION

9 We have shown that combining physical sintering with chemical sintering using nanoglu
10 particles enhances nanocrystalline particle interconnectivity within TiO₂ electrodes of dye solar
11 cells. This approach has been applied for the preparation of photoanodes on a conductive
12 ITO/PEN substrate for the generation of highly efficient plastic DSCs. The effect of compression
13 on the structural and photovoltaic properties of the plastic DSCs was thoroughly investigated and
14 rationalized. The electron transport resistance in compressed TiO₂ films gradually decreased as
15 the applied pressure increased from 0 MPa to 100 MPa, revealing the enhanced interconnectivity
16 of TiO₂ nanoparticles. Furthermore, the improved electron diffusion coefficient, electron
17 diffusion length, and charge-collection efficiency were also studied for TiO₂ films prepared
18 under different conditions. State-of-the-art cells on plastic substrates displaying power
19 conversion efficiencies of 6.4% were realized employing widely-used and commercial-available
20 P25 particles to prove the feasibility of the proposed method. Future work should focus on the
21 optimization of the optical design of the cell to maximize light harvesting, as well as on the
22 preparation of a fully flexible solar cell based on this synergic concept.

23

1 ***Corresponding Authors:**

2 Dr. Min Jae Ko, Tel.: +82-2-958-5518. Fax: +82-2-958-6649. E-mail: mjko@kist.re.kr

3 Dr. Hernán Míguez, Tel.: +34-954-489-581. Fax: +34-954-460-665. E-mail: h.miguez@csic.es

4 ‡These authors contribute equally to this work

5 **ACKNOWLEDGEMENT**

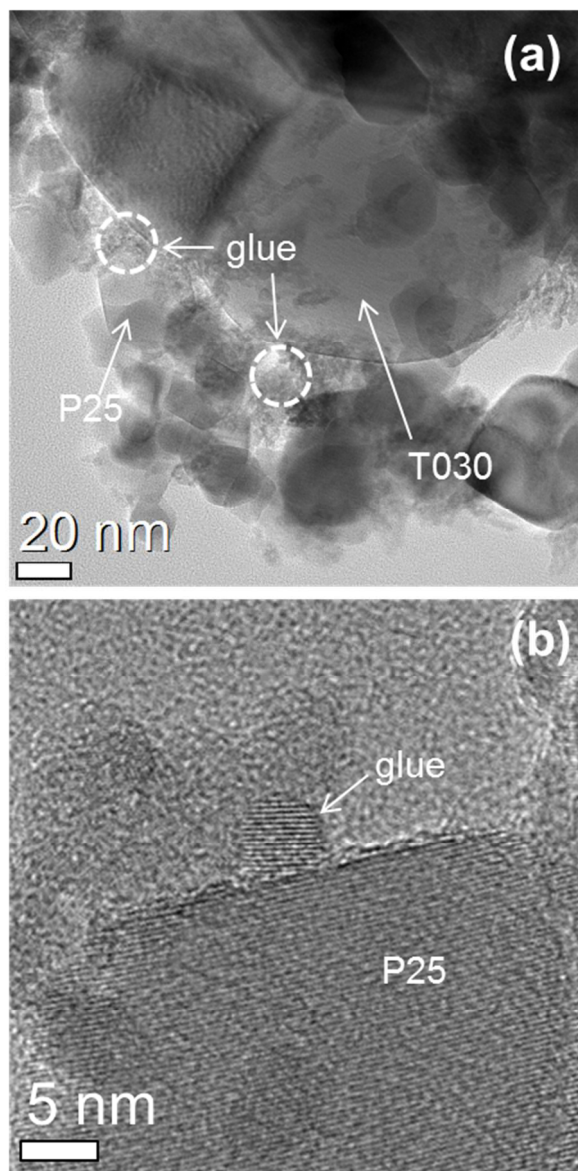
6 MJK acknowledge funding support from the Global Frontier R&D Program on Center for
7 Multiscale Energy System (2012M3A6A7054856) and 2015 University-Institute cooperation
8 program funded by the National Research Foundation under the Ministry of Science, ICT &
9 Future Planning, Korea; This work was also supported by the KIST institutional programs. YL
10 acknowledges the financial support by a Marie Curie International Incoming Fellowship within
11 the 7th European Community Framework Programme under grant agreement number of PIIF-
12 GA-2013-622533. HM acknowledges funding from the European Research Council under the
13 European Union's Seventh Framework Programme (FP7/2007-2013)/ERC grant agreement n°
14 307081 (POLIGHT) and the Spanish Ministry of Economy and Competitiveness under grant
15 MAT2011-23593.

16

1 REFERENCES

- 2 1. T. Miyasaka, M. Ikegami and Y. Kijitori, *Journal of the Electrochemical Society*, 2007,
3 **154**, A455-A461.
- 4 2. T. Yamaguchi, N. Tobe, D. Matsumoto and H. Arakawa, *Chemical Communications*,
5 2007, 4767-4769.
- 6 3. X. Li, H. Lin, J. Li, N. Wang, C. Lin and L. Zhang, *Journal of Photochemistry and*
7 *Photobiology a-Chemistry*, 2008, **195**, 247-253.
- 8 4. N. G. Park, K. M. Kim, M. G. Kang, K. S. Ryu, S. H. Chang and Y. J. Shin, *Advanced*
9 *Materials*, 2005, **17**, 2349.
- 10 5. Y. Li, W. Lee, D. K. Lee, K. Kim, N. G. Park and M. J. Ko, *Applied Physics Letters*,
11 2011, **98**.
- 12 6. Y. Li, K. Yoo, D.-K. Lee, J. Y. Kim, H. Kim, B. Kim and M. J. Ko, *Nanoscale*, 2013, **5**,
13 4711-4719.
- 14 7. H. C. Weerasinghe, P. M. Sirimanne, G. V. Franks, G. P. Simon and Y. B. Cheng,
15 *Journal of Photochemistry and Photobiology a-Chemistry*, 2010, **213**, 30-36.
- 16 8. H. Lindstrom, E. Magnusson, A. Holmberg, S. Sodergren, S. E. Lindquist and A.
17 Hagfeldt, *Solar Energy Materials and Solar Cells*, 2002, **73**, 91-101.
- 18 9. J. Halme, J. Saarinen and P. Lund, *Solar Energy Materials and Solar Cells*, 2006, **90**,
19 887-899.
- 20 10. X. Zhao, H. Lin, X. Li and J. Li, *Electrochimica Acta*, 2011, **56**, 6401-6405.
- 21 11. Z. Dongshe, T. Yoshida, T. Oekermann, K. Furuta and H. Minoura, *Advanced Functional*
22 *Materials*, 2006, **16**, 1228-1234.
- 23 12. H.-Y. Jin, J.-Y. Kim, J. A. Lee, K. Lee, K. Yoo, D.-K. Lee, B. Kim, J. Y. Kim, H. Kim,
24 H. J. Son, J. Kim, J. A. Lim and M. J. Ko, *Applied Physics Letters*, 2014, **104**, 43902-
25 43902.
- 26 13. H. C. Weerasinghe, F. Huang and Y.-B. Cheng, *Nano Energy*, 2013, **2**, 174-189.
- 27 14. H.-P. Jen, M.-H. Lin, L.-L. Li, H.-P. Wu, W.-K. Huang, P.-J. Cheng and E. W.-G. Diau,
28 *Acs Applied Materials & Interfaces*, 2013, **5**, 10098-10104.
- 29 15. M. J. Yun, S. I. Cha, S. H. Seo and D. Y. Lee, *Scientific Reports*, 2014, **4**, 5322.
- 30 16. T. Yamaguchi, N. Tobe, D. Matsumoto, T. Nagai and H. Arakawa, *Solar Energy*
31 *Materials and Solar Cells*, 2010, **94**, 812-816.
- 32 17. H. Arakawa, T. Yamaguchi, T. Sutou, Y. Koishi, N. Tobe, D. Matsumoto and T. Nagai,
33 *Current Applied Physics*, 2010, **10**, S157-S160.
- 34 18. H.-W. Chen, C.-Y. Hsu, J.-G. Chen, K.-M. Lee, C.-C. Wang, K.-C. Huang and K.-C. Ho,
35 *Journal of Power Sources*, 2010, **195**, 6225-6231.
- 36 19. K. D. Benkstein, N. Kopidakis, J. van de Lagemaat and A. J. Frank, *Journal of Physical*
37 *Chemistry B*, 2003, **107**, 7759-7767.
- 38 20. J. van de Lagemaat, K. D. Benkstein and A. J. Frank, *Journal of Physical Chemistry B*,
39 2001, **105**, 12433-12436.
- 40 21. D. Bouvard and F. F. Lange, *Physical Review A*, 1992, **45**, 5690-5693.
- 41 22. K. Fan, C. Gong, T. Peng, J. Chen and J. Xia, *Nanoscale*, 2011, **3**, 3900-3906.
- 42 23. X. Li, H. Lin, J. Li, X. Li, B. Cui and L. Zhang, *Journal of Physical Chemistry C*, 2008,
43 **112**, 13744-13753.
- 44 24. A. G. Agrios and A. Hagfeldt, *Journal of Physical Chemistry C*, 2008, **112**, 10021-10026.
- 45 25. J. Bisquert, *Journal of Physical Chemistry B*, 2002, **106**, 325-333.

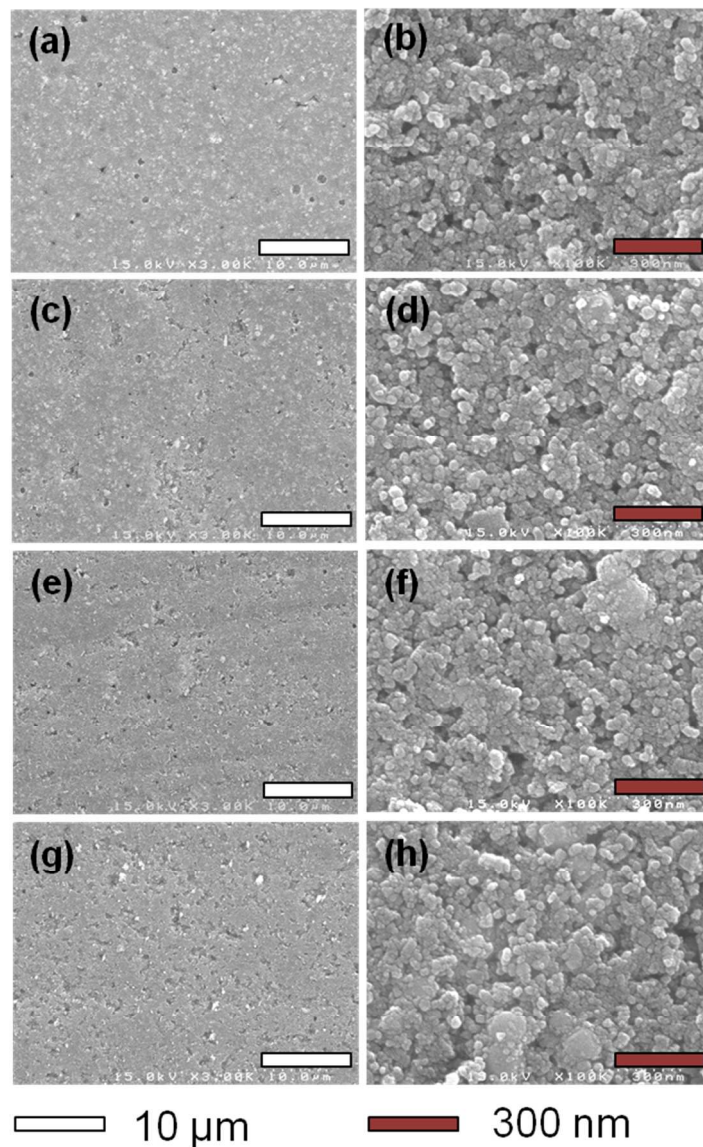
- 1 26. F. Fabregat-Santiago, J. Bisquert, G. Garcia-Belmonte, G. Boschloo and A. Hagfeldt,
2 *Solar Energy Materials and Solar Cells*, 2005, **87**, 117-131.
- 3 27. T. Hoshikawa, M. Yamada, R. Kikuchi and K. Eguchi, *Journal of the Electrochemical*
4 *Society*, 2005, **152**, E68-E73.
- 5 28. M. Adachi, M. Sakamoto, J. Jiu, Y. Ogata and S. Isoda, *Journal of Physical Chemistry B*,
6 2006, **110**, 13872-13880.
- 7 29. J. Bisquert, G. Garcia-Belmonte, F. Fabregat-Santiago, N. S. Ferriols, P. Bogdanoff and
8 E. C. Pereira, *Journal of Physical Chemistry B*, 2000, **104**, 2287-2298.
- 9 30. Q. Wang, S. Ito, M. Graetzel, F. Fabregat-Santiago, I. Mora-Sero, J. Bisquert, T. Bessho
10 and H. Imai, *Journal of Physical Chemistry B*, 2006, **110**, 25210-25221.
- 11 31. Q. Wang, Z. Zhang, S. M. Zakeeruddin and M. Graetzel, *Journal of Physical Chemistry*
12 *C*, 2008, **112**, 7084-7092.
- 13 32. J. Bisquert, F. Fabregat-Santiago, I. Mora-Sero, G. Garcia-Belmonte and S. Gimenez,
14 *Journal of Physical Chemistry C*, 2009, **113**, 17278-17290.
- 15 33. F. Fabregat-Santiago, J. Bisquert, L. Cevey, P. Chen, M. Wang, S. M. Zakeeruddin and
16 M. Graetzel, *Journal of the American Chemical Society*, 2009, **131**, 558-562.
- 17 34. S. Nakade, M. Matsuda, S. Kambe, Y. Saito, T. Kitamura, T. Sakata, Y. Wada, H. Mori
18 and S. Yanagida, *Journal of Physical Chemistry B*, 2002, **106**, 10004-10010.
- 19 35. H.-W. Chen, Y.-T. Liao, J.-G. Chen, K. C. W. Wu and K.-C. Ho, *Journal of Materials*
20 *Chemistry*, 2011, **21**, 17511-17518.
- 21 36. A. R. Pascoe, F. Huang, N. W. Duffy and Y.-B. Cheng, *Journal of Physical Chemistry C*,
22 2014, **118**, 15154-15161.
- 23
- 24
- 25
- 26
- 27
- 28



1

2

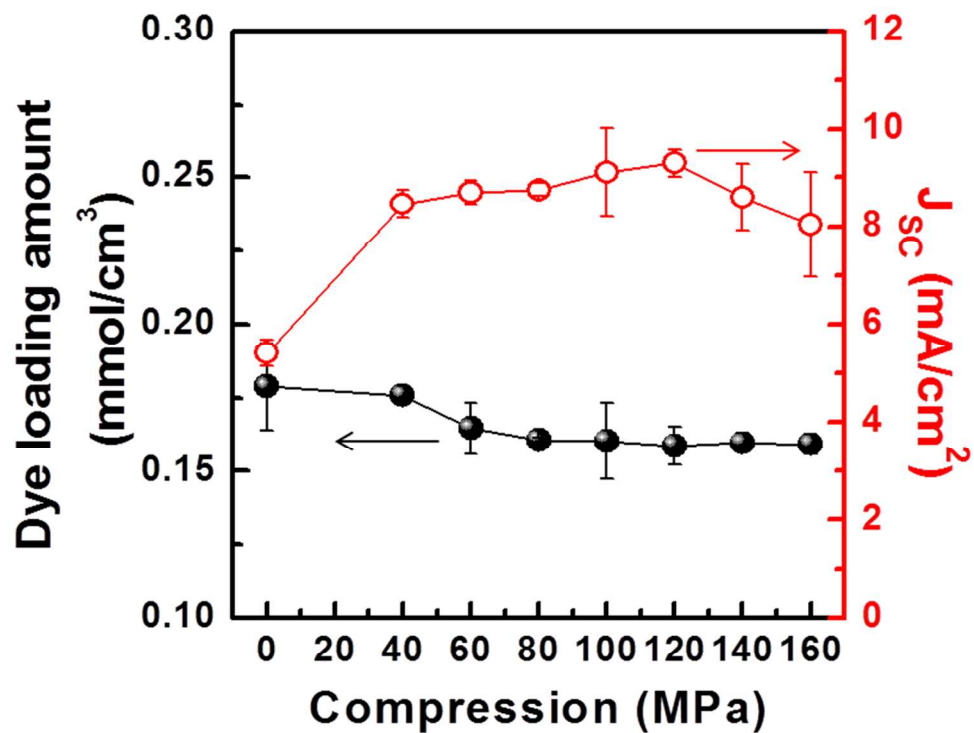
3 Figure 1 TEM images of TiO₂ films that were partially removed from the substrate prior to
4 compression (a) and enlarged image (b).

1
2
3

4

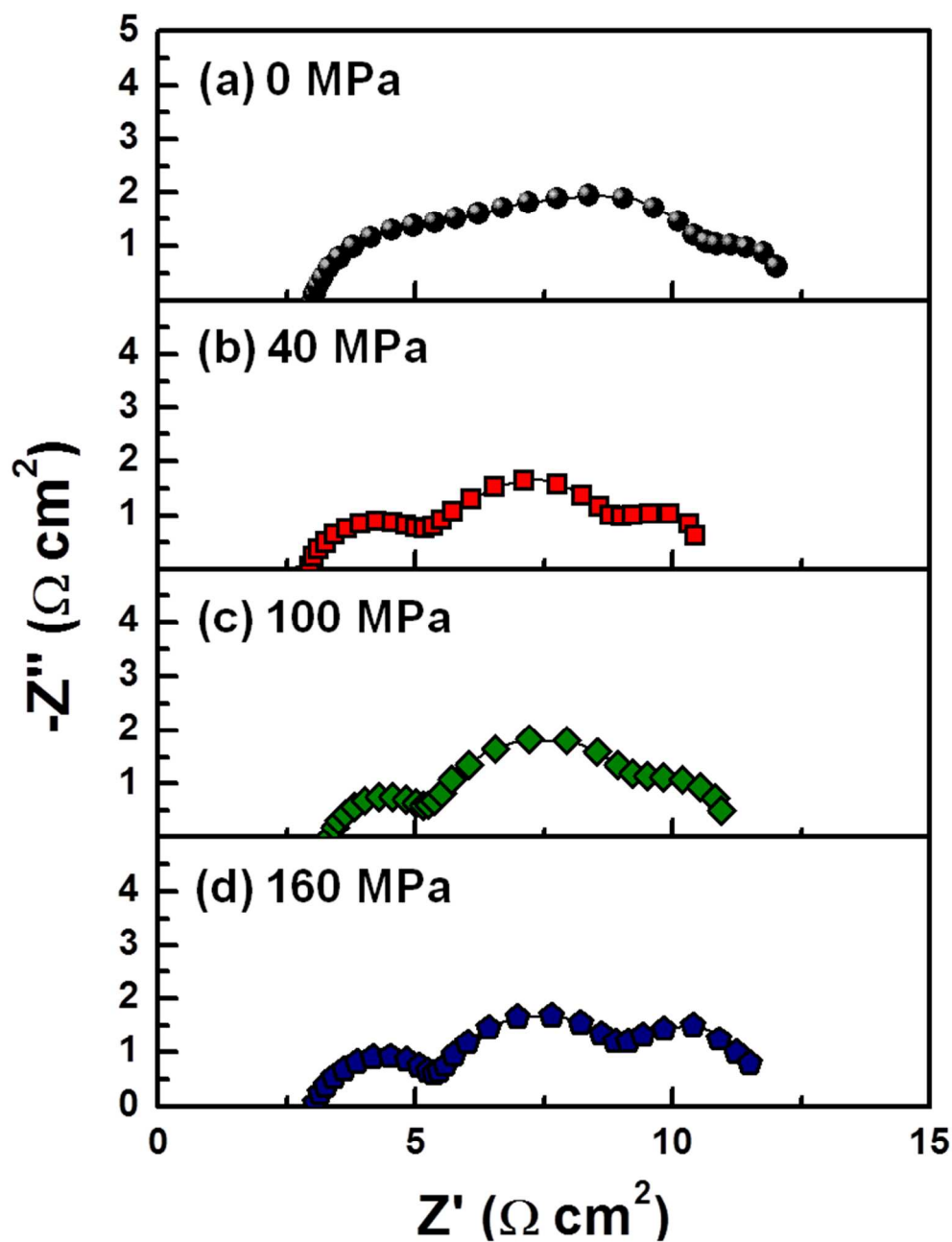
5 Figure 2 SEM images of films pressed with various compression forces showing film
6 morphologies and structures. For comparison, films prepared with a compression pressure of 0
7 MPa (a, b), 40 MPa (c, d), 100 MPa (e, f), and 160 MPa (g, h) are observed. The images in the
8 left column are of surface morphologies and those in the right column are of cross-section
9 morphologies.

10



1
2 Figure 3 The dye loading amount for films compressed with various compression forces. For
3 comparison, the averaged J_{sc} from three cells made of same condition was also plotted.

4
5
6
7
8
9
10
11
12
13
14
15

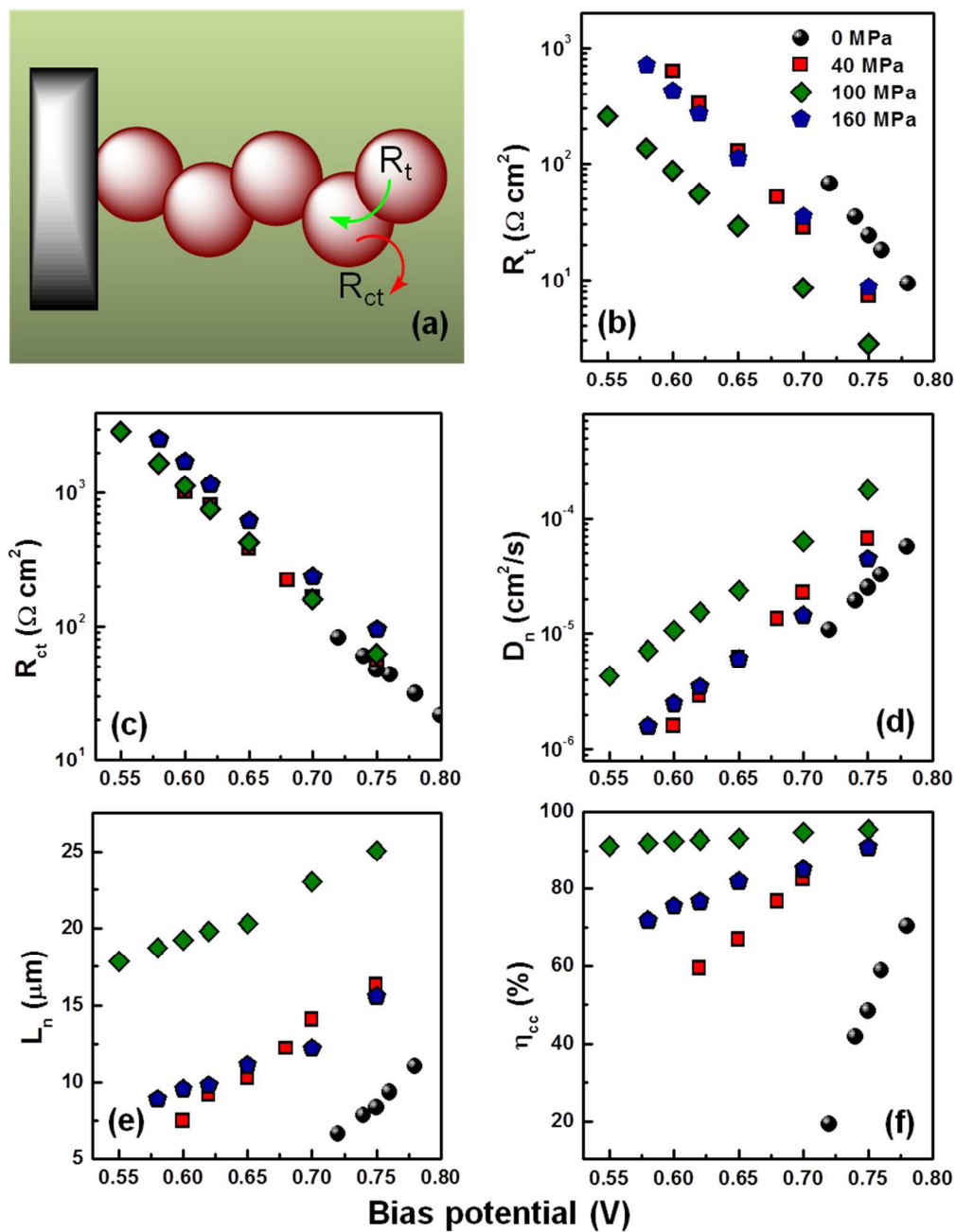


1
2

3 Figure 4 Nyquist plots of impedance spectra from cells prepared with compression forces of 0
4 MPa, 40 MPa, 100 MPa, and 160 MPa; spectra were recorded at one-sun illumination with open
5 circuit condition.

1

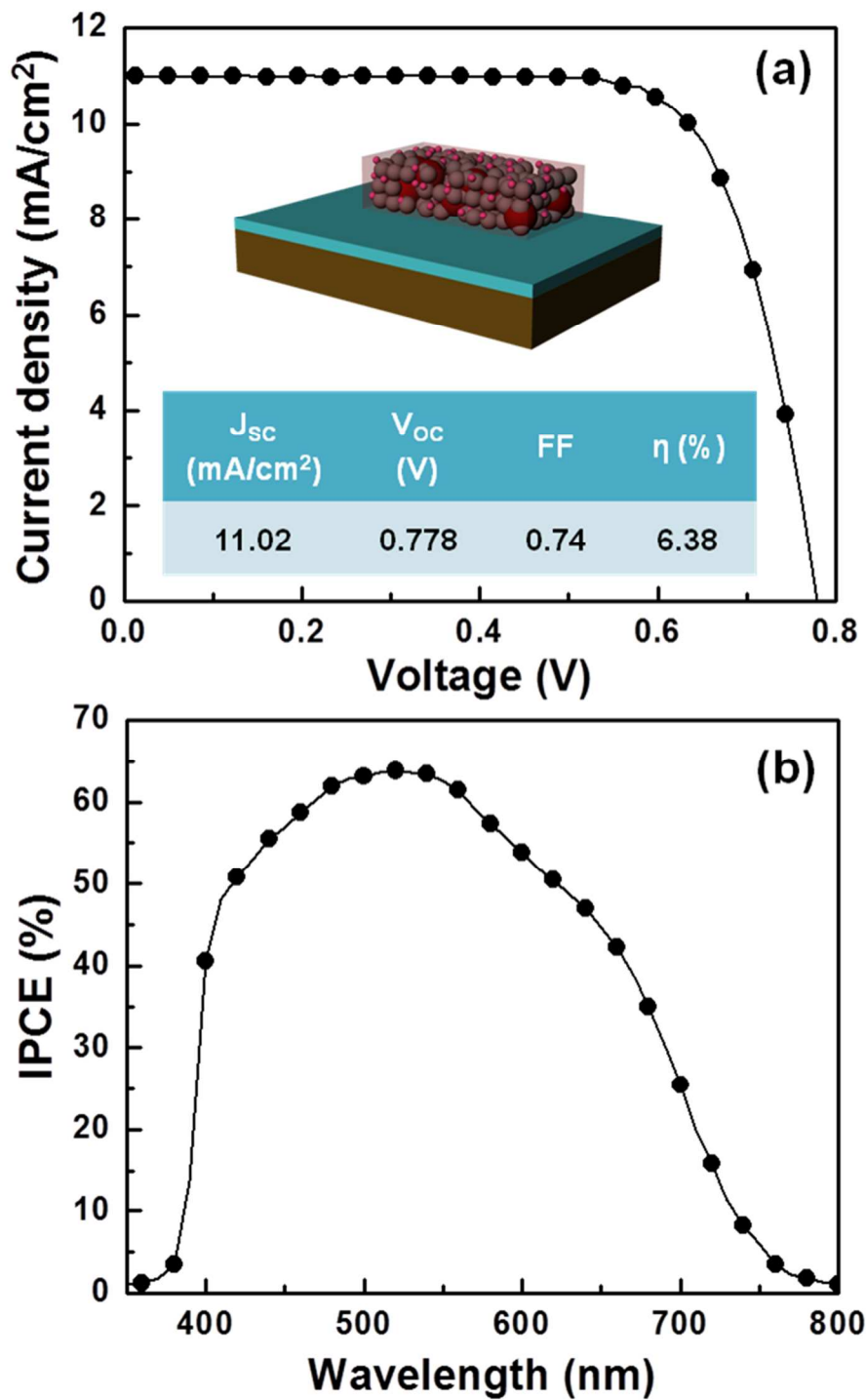
2



3

4 Figure 5 Schematic of electron transport and recombination (a). The fitted R_t (b), R_{ct} (c) and
 5 calculated D_n (d), L_n (e), η_{cc} (f) of compressed films at various compression forces as measured in
 6 the dark by electrochemical impedance spectroscopy.

7



1
2 Figure 6 The current–voltage curve (a) and IPCE (b) of the optimized cell with TiO₂ film
3 thickness of 8.72 μm . The schematic of the films' structure and composition is presented in inset
4 along with the summarized photovoltaic properties.

5

1 Table 1 Photovoltaic properties of cells compressed with various compression forces. The
2 electrolyte is composed of 0.7 M PMII, 0.03 M I2, 0.05 M GuSCN and 0.5 M tBP in a mixture
3 of acetonitrile and valeronitrile (v/v = 85:15). The data is averaged from at least three points.

4

Sample	J_{sc} (mA/cm ²)	V_{oc} (V)	FF	η (%)
0 MPa	5.42 ± 0.26	0.778 ± 0.005	0.68 ± 0.01	2.86 ± 0.16
40 MPa	8.46 ± 0.29	0.788 ± 0.007	0.70 ± 0.01	4.66 ± 0.21
60 MPa	8.68 ± 0.24	0.793 ± 0.004	0.69 ± 0.02	4.78 ± 0.13
80 MPa	8.75 ± 0.13	0.786 ± 0.007	0.70 ± 0.01	4.82 ± 0.10
100 MPa	9.64 ± 0.04	0.797 ± 0.003	0.69 ± 0.01	5.31 ± 0.10
120 MPa	9.29 ± 0.28	0.796 ± 0.008	0.70 ± 0.01	5.18 ± 0.17
140 MPa	8.59 ± 0.68	0.794 ± 0.014	0.68 ± 0.01	4.67 ± 0.38
160 MPa	8.03 ± 1.07	0.798 ± 0.021	0.71 ± 0.02	4.54 ± 0.48

5

6